Stabilization of ferromagnetism via structural modulations in Cr-doped CaRuO₃:
A neutron diffraction and Raman spectroscopy study

Pooja [1,*] K. S. Chikara [2,3] Aprajita [4] Sachindra Nath Sarangi [5] D. Samal [5,3] Surajit Saha [4] A. K. Bera [2,3]
S. M. Yusuf [2,3] and Chanchal Sow [1,†]

[1] *Department of Physics, Indian Institute of Technology, Kanpur 208016, India*
[2] *Solid State Physics Division, Bhabha Atomic Research Centre, Mumbai 400085, India*
[3] *Homi Bhabha National Institute, Anushaktinagar, Mumbai 400094, India*
[4] *Department of Physics, Indian Institute of Science Education and Research, Bhopal 462066, India*
[5] *Institute of Physics, Bhubaneswar 751005, India*

The magnetic ground state of CaRuO₃ is mystifying as it is poised on the verge of a quantum critical point. Minute perturbations via strain, chemical doping (or inhomogeneity or protonation), temperature, etc., alter the magnetic ground state of the system. The unit cell volume gets squeezed by 0.6% with 15% Cr doping in CaRuO₃. Here we study temperature-dependent neutron diffraction, neutron depolarization, magnetization, and Raman spectroscopy to understand the magnetism and its correlation with crystal structure. The bulk magnetization data indicate a possible weak ferromagnetic order below 100 K, which is well supported by the spin-phonon coupling below T_C. Finally, the neutron depolarization analysis confirms about the ferromagnetic ground state below 100 K in 15% Cr-doped CaRuO₃. The effect of Cr doping in combination with temperature-dependent structural modulations found to be the origin of ferromagnetism in CaRuO₃.

I. INTRODUCTION

Investigation of low-temperature structural and magnetic coupling in functional ABO_3 perovskite-type oxides is an attractive area for research and applications [1]. The adjustment between electron-electron interactions, spin-orbit coupling (SOC), and crystal field (CF) gives rise to several complex magnetic ground states in perovskite oxides [2–5]. In addition, the ability to tailor the physical properties by adjusting external parameters such as pressure, temperature, and chemical doping makes perovskites incredibly valuable. These external perturbations induce various structural distortions such as rotation of BO_6 octahedra [6], polar ion displacement (induced ferroelectricity) [7], and octahedra distortions (Jahn-Teller distortion) [8]. There are two most prevalent structures in perovskites: $R − 3c$ with tilt system $a^-a^-a^-$ (Glazer's notation [9]) and $Pnma$ with tilt $a^-b^+a^-$. Particularly interesting Ru-based perovskites are the members of strongly correlated systems with the orthorhombic $Pnma$ structure [10]. The orthorhombic distortion, driven by octahedral tilting and rotation, can be significantly adjusted by varying the ionic size, which in turn alters both the B-O-B bond angle and the B-O bond length. The structural deformation and its effect on the electric, magnetic, and spectroscopic characteristics are adequately demonstrated in the Ru-based perovskite CaRuO₃ [10,11]. Reports found that the CRO is near to the Mott insulator transition boundary [12,13]. Even though SrRuO₃

and CaRuO₃ both possess similar electronic properties, both have different magnetic ground states. The magnetic ground state of CaRuO₃ is controversial to date, being poised among paramagnetic (PM) [14], ferromagnetic (FM) [15], and antiferromagnetic (AFM) [5]. Such questionable magnetic ground states can also be tuned by chemical doping. An extensive study on chemical doping of Ru ion has been found to destroy the magnetic ground state in CaRuO₃ [10,16–18]. The more relevant example, the evolution of itinerant ferromagnetism in $Ca_xSr_{1-x}RuO_3$, has been found due to mismatch in the ionic radius of Sr^{2+} (0.131 nm) and Ca^{2+} (0.118 nm) at the same site, causing the change in octahedral bond angles [19]. Moreover, various reports with different $3d$ transition-metal ions (Fe^{3+}, Mn^{4+}, Co^{2+}, Ni^{2+}, Cr^{3+}, and Cu^{2+}) doping in CaRuO₃ have been found [20–24]. Among all $3d$ ions, Cr doping is the most enthralling as it contains unpaired d electron and induces relatively larger magnetic moment per formula unit than the same amount of Fe doping in CaRuO₃ [20,22]. It has been also found that Cr doping results in the spin glass behavior and improved magnetic correlations in CaRuO₃ [25,26]. In addition, several interesting physical properties are exhibited by chromium containing oxides, such as the half-metallicity of CrO_2 and the induced ferromagnetism in $Ln_{0.5}Ca_{0.5}Mn_{1-x}Cr_xO_3$ manganites. Recently, the $\sim$30 K enhancement of T_C in SrRuO₃, has been observed by the Cr doping at Ru site [27]. The origin of this T_C enhancement is found to be the structural modulation [28]. In the more recent work, the exception found FM order with tiny (1%) Cr doping and reaches maximum $T_C \sim 100$ K at 15% in CaRuO₃ [22,29]. However, there are still some unanswered questions in Cr-doped CaRuO₃, concerning the role of structural

modulation close to the phase transition and nonsaturating low magnetic moment (five times smaller than the isostructural Cr-doped $SrRuO_3$ [28]). These features motivate us to perform a detailed low-temperature structural, magnetic, and spectroscopic study in Cr-doped $CaRuO_3$. A powerful technique such as neutron powder diffraction (NPD) is highly useful here [30]. The NPD gives the microscopic picture of magnetic and crystal structural parameters. For a detailed understanding of the magnetic inhomogeneous system as well as domain magnetization, the neutron depolarization (ND) method is employed, which provides the domain magnetic correlations in the mesoscopic length (10–1000 nm) scale [31]. In a magnetically inhomogeneous system, where spin fluctuations and internal domain magnetization are present, the neutron beam's spin polarization is impacted, resulting in a depolarization effect [32]. Several studies have demonstrated a high sensitivity of neutron polarization to the presence of ferromagnetic domains [31,33]. It has long been understood that minor ferromagnetic fluctuations within a paramagnetic host can lead to the depolarization of a neutron beam [34,35]. This study aims to clarify the nature of spin dynamics and magnetic correlation in Cr-doped $CaRuO_3$. It also sheds light on the magnetism that drives the atypical magnetic properties of $CaRuO_3$. On the other hand, Raman spectroscopy is the optical technique that probes vibrational, rotational, and other low-energy dynamics in the material. It is an advantageous technique to probe the structural distortion, and magnetostructural (spin-phonon) coupling in the system [36,37]. By measuring the change in Raman shift (ω_{ph}) (inelastic scattering) of incident monochromatic light wave, we get the idea of change in Raman modes. The Raman modes are associated with the crystal structure symmetry and atomic vibrations [38]. The behavior of ω_{ph}, showing either a decrease or increase, has been observed in magnetically ordered materials, such as ferromagnetic $SrRuO_3$ [39]. This effect arises from the modulation of the spin-spin exchange integral by lattice vibrations. In Cr-doped $CaRuO_3$, Raman spectroscopy provides insights into the correlations between magnetic ordering and crystal structure.

This paper presents a detailed structural, spectroscopic, magnetic, and temperature-dependent NPD and ND of Cr-doped $CaRuO_3$ compared with the parent compound. The temperature-dependent crystal structural evolution finds a sharp change in lattice parameter and a stable peak in unit cell volume exactly at $T_C \sim 100$ K at 15% Cr-doped $CaRuO_3$. However, the parent compound skips such structural changes. Further, the Raman frequency deviation from the anharmonic contribution and finite neutron depolarization below $T_C \sim 100$ K is stabilized by the strong coupling between crystal structural distortion and magnetic ordering in Cr-doped $CaRuO_3$.

II. EXPERIMENTAL DETAILS

A single-phase $CaRu_{1-x}Cr_xO_3$ (CRCO) sample with ($0 \leqslant$ x $\leqslant 0.15$) is prepared by standard solid-state ceramic method. The samples are characterized by room temperature (RT) neutron powder diffraction (NPD) measurement and Rietveld analysis. The details of sample preparation and x-ray diffraction (XRD) analysis are given in Ref. [29]. The Raman spectra

of all different samples are collected with LabRAM HR Evolution Raman spectrometer in the backscattering geometry. A Peltier cooled charge coupled device (CCD) is used to detect the Raman signal. The temperature of the sample is varied using the Linkam heating stage (Model HFS600E-PB4). The excitation source of 532 nm is used to illuminate the samples at different laser powers. The crystalline quality and composition of the samples are checked by the high-resolution transmission electron microscopy (HRTEM) using TITAN X-FEG at 300 eV. The NPD is performed on CRO ($x = 0$) and CRCO15 ($x = 0.15$) samples using the three linear position sensitive detector-based neutron Powder Diffractometer-I (PD-1) with a wavelength of 1.094 Å, located at the Dhruva Research Reactor at Bhabha Atomic Research Centre (BARC) in Mumbai, India [40]. The NPD patterns are recorded over the 2θ range 5–70 degrees, corresponding to a Q range (where $Q = 4\pi \sin\theta/\lambda$) of 0.4–6.5 Å^{-1}, at several temperatures from 5–300 K. For NPD measurements, the powder samples are filled in a cylindrical vanadium container (diameter $\sim$6 mm) and attached to the cold finger of a helium-4-based vertical closed cycle refrigerator (CCR). The vanadium container containing the powder samples is thermalized for $\sim$30 min at each temperature before the recording of the diffraction patterns. The experimentally measured neutron diffraction patterns are analyzed by the Rietveld refinement method using the FULLPROF suite [41] computer program. The one-dimensional neutron depolarization (ND) measurements on the CRO and CRCO15 compounds are carried out using the polarized neutron spectrometer (PNS) ($\lambda = 1.205$ Å) also located at Dhruva reactor, BARC [42]. For ND measurements, the samples are first cooled from RT down to 2 K by using a helium-4-based CCR in the presence of a 35 Oe applied field, which is required to maintain the neutron beam polarization at the sample position. The transmitted neutron beam polarization is measured as a function of sample temperature in the warming cycle under the same value of the applied external magnetic field. Magnetization measurement is performed using a superconducting quantum interference device (SQUID) magnetometer (MPMS).

III. RESULTS AND DISCUSSION

A. Crystal structure

Figures 1(a) and 1(d) depict the HRTEM image of μm-sized crystals of CRO and CRCO15, respectively. The selected area image obtained from HRTEM is shown in Figs. 1(b) and 1(e), showing the periodic fringes of the crystal lattice of CRO and CRCO15, respectively, under the same experiential condition. Such periodic fringes verify the crystalline nature. The distance between the crystalline plane is 4.16(3) Å and 4.15(2) Å for CRO and CRCO15, corresponding to the (101) plane at 2θ angle of 23.16°. The diffraction spot of the (101) plane is seen in the selected area electron diffraction pattern of both samples [inset Fig. 1(c) and 1(f)]. The high angle annular dark field (HAADF) image of CRO and CRCO15 depicts the crystal size of $\sim$400 nm in both cases, as shown in Figs. 1(c) and 1(f). The HAADF element mapping further confirms the desired composition of the constituent elements (not shown here) in
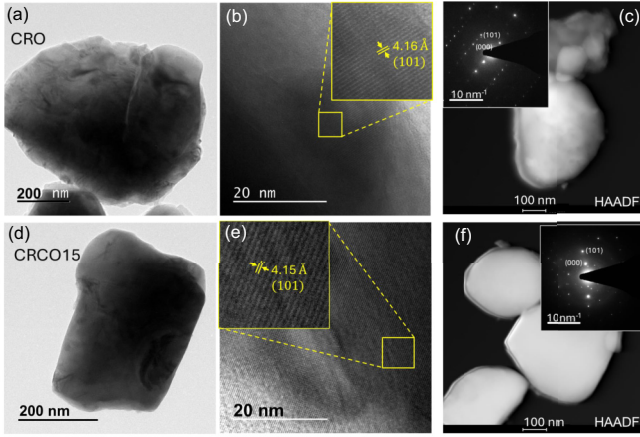
FIG. 1. (a), (d) HRTEM image of μm-sized crystals of CRO (circular shaped) and CRCO15 (rectangular shaped). (b), (e) Selected area pattern, and (c), (f) HAADF images of CRO (top image) and CRCO15 (bottom image). The inset of (b) and (e) shows the zoomed-in view of the square region. Whereas the inset of (c) and (f) depicts the selected area diffraction pattern of corresponding samples.

the system. Further, the crystal structure symmetry and lattice parameters of the samples are evaluated through the NPD measurement at RT.

Figure 2(a) depicts the experimentally measured and calculated RT NPD patterns of CRO and CRCO15. Rietveld analysis reveals that both CRO and CRCO15 have orthorhombic crystal symmetry with space group *Pnma* (62). The derived values of lattice parameters at RT for both compounds are tabulated in Table I. The lattice parameters closely agreed with the parameters evaluated from the RT XRD data. The CRCO15 compound has a lower unit cell volume ($\sim$1.0%) and orthorhombicity factor (a/c) ($\sim$0.6%) than the parent compound CRO. The origin of such reduced unit cell volume in CRCO15 is the smaller ionic radii of Cr^{6+}(0.044 nm)/Cr^{3+}(0.062 nm) (the oxidation state of Cr has been confirmed by x-ray photoelectron microscopy) than that of the Ru^{4+} (0.062 nm) ion. The change in unit cell volume and a/c ratio with Cr doping, suggests the stabilization of structural distortion in CRO. The schematic view of the orthorhombic crystal structure of CRCO15 is shown in Fig. 2(b). The crystal structure consists of the corner sharing $(Ru/Cr)O_6$ octahedron along all three crystallographic directions. Each of these octahedra possesses tilt along the in-plane (IP) and out-of-plane (OP) directions leading to deviation of the Ru-O-Ru bond angles from 180 degrees. Figure 2(c) demonstrates
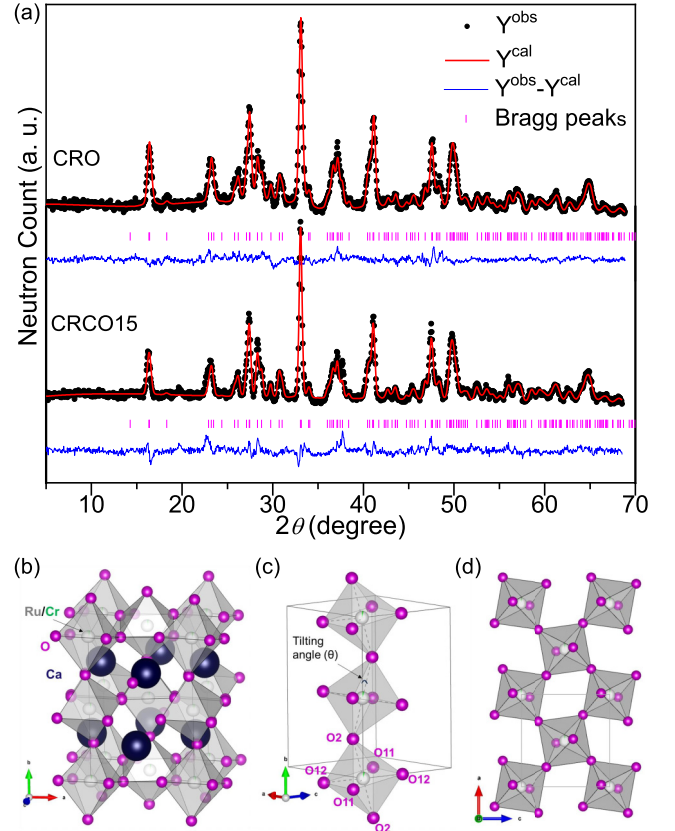

FIG. 2. (a) Room temperature NPD pattern of the parent and the 15% Cr-doped compounds. The solid black circles and red continuous lines are measured data points and calculated patterns, respectively. The blue lines at the bottom of each panel show the difference between measured and calculated patterns. The pink vertical bars are allowed Bragg peak positions. (b) The crystal structure of 15% Cr-doped sample, obtained using VESTA visualizing program [43], after the Reitveld refinement. (c) Side view of the unit cell containing $(Ru/Cr)O_6$ octahedra to demonstrate the octahedral tilt and various oxygen atoms (apical O2 in *bc* plane, and basal O11, O12 in *ac* plane). (d) Two-dimensional (2D) (*ac* plane) view of crystal structure to visualize IP rotation of the octahedra. The gray solid line represents the unit cell dimension.

the octahedral tilt ($\theta = 180 - \angle$Ru-O-Ru, along the *b* axis) and various oxygen atoms O2 (apical) and O11, O12 (basal). In addition to the OP tilt, the $(Ru/Cr)O_6$ octahedron also possesses the IP rotation as depicted in Fig. 2(d). The distortion of octahedra results the unequal Ru-O bond lengths:

TABLE I. The derived lattice parameters at 300 and 5 K obtained from Rietveld analysis of NPD patterns.

Compounds	300 K		5 K	
	CRO	CRCO15	CRO	CRCO15
a (Å)	5.5074(4)	5.4798(7)	5.5087(7)	5.4867(3)
b (Å)	7.6625(6)	7.6450(9)	7.6522(0)	7.6328(5)
c (Å)	5.3731(3)	5.3580(6)	5.3576(6)	5.3484(3)
V (Å^3)	226.753(3)	224.469(5)	225.845(5)	223.988(2)

TABLE II. List of Raman shift frequency (ω_{ph}) and their corresponding symmetry modes for Raman active phonons in CRO and CRCO15. Best compare with the reported ω_{ph} values of CaRuO$_3$.

Peaks	Symmetry modes	$\omega_{ph}^{CaRuO_3}$ [45]	ω_{ph}^{CRO}	ω_{ph}^{CRCO15}	Atomic motions involved
P1	$A_g(1)$, $B_{2g}(1)$	172	143 ± 1.0	167 ± 0.4	RuO$_6$ y rotation and breathing
P2	$A_g(3)$	268	223 ± 1.4	255 ± 0.5	RuO$_6$ rotation/stretching
P3	$A_g(5)$	357	328 ± 2.1	350 ± 0.5	Ca(x), RuO$_6$ stretching/bending
P4	$A_g(6)$	418	387 ± 2.6	416 ± 1.1	O1-Ru-O1,O2-Ru-O2 bendings
P5	$B_{2g}(5)$	447	419 ± 0.7	444 ± 0.5	O1-Ru-O1,O2-Ru-O2 bendings
P6	$A_g(7)$	557	534 ± 0.7	560 ± 0.4	Ru-O2 in-plane stretching
P7	$B_{2g}(1)$	616	668 ± 0.8	639 ± 1.1	Ru-O2 stretching (breathing)
P8	–	737	698 ± 0.7	739 ± 0.9	–

Ru-O2 (apical), Ru-O11 (basal), and Ru-O12(basal). The octahedral distortions are quantified in terms of stretching distortions (Δ) and angular distortions (Σ) [44], have been calculated as:

$$\Delta = \frac{1}{6} \Sigma_{i=1}^{6} \left[\frac{|d_i - d_{mean}|}{d_{mean}} \right]^2, \qquad (1)$$

$$\Sigma = \frac{1}{12} \Sigma_{i=1}^{12} |\phi_i - 90|, \qquad (2)$$

respectively. Here d_{mean} and d_i denote the average and ith (Ru/Cr)-O bond length respectively. The angle ϕ_i is considered as ith O-(Ru/Cr)-O bond angles in the (Ru/Cr)O$_6$ octahedron. The value of θ and Δ increases by $\sim 6°$ and 18 times, respectively, for 15% Cr doping in CRO. The calculated value of Σ, Δ, and θ for CRO and CRCO15 at different temperatures is discussed in the temperature-dependent NPD section below. The unequal bond lengths and octahedral distortion make CRCO an interesting candidate for the Raman study.

B. Raman spectroscopy

In cubic perovskite ABO_3, Raman scattering is forbidden by the BO_6 octahedron symmetry. Whereas in orthorhombic *Pnma* perovskite structure, the antiphase tilt of adjacent BO_6 octahedron (a$^-$b$^+$a$^-$ in Glazer's notation [9]) breaks the cubic symmetry and thus activates the Raman modes. According to the group theory, ABO_3 perovskite system [space group = *Pnma*, Z = 4 (four formula units per unit cell)] has 60 Γ-point phonons; 24 of them are Raman active ($7A_g + 15B_{1g} + 17B_{2g} + 15B_{3g}$) and 25 are infrared active ($9B_{1u} + 17B_{2u} + 19B_{3u}$) modes [45–47]. In parent compound CRO the $A_g(1)$, $A_g(3)$, and $A_g(5)$ modes arise due to the movement of Ca atoms, whereas $A_g(6)$ and $B_{2g}(5)$ modes involve OP and IP octahedral tilting and banding. Similarly, $A_g(7)$ and $B_{2g}(1)$ are related to the (Ru/Cr)-O bond length stretching and breathing along IP and OP, respectively. There is a complex band around and above 700 cm^{-1}, which is assumed to have a phonon density of state origin [45]. The particular symmetry mode of atomic vibration at a different value of Raman shift frequency (ω_{ph}) corresponds to a particular peak, named P1–P8 (are tabulated in Table II). The RT Raman spectra of CRCO samples are shown in Fig. 3(a). Each of the Raman spectra can be deconvoluted into eight Lorentzian functions identifying the various phonon modes (peaks P1–P8) as shown in Fig. 3(b). The value of ω_{ph} for the parent compound CRO is closely agreed with

the experimentally and theoretically derived values [45] (see Table II). There is no change in the spectral characteristics (in the form of peak emergence or disappearance) in the Raman spectra of CRCO. However, the value of ω_{ph} is changed on changing the Cr concentration in CRO. Figure 3(c) shows the variation of ω_{ph} and linewidth of peaks: P1 (168 Cm^{-1}), P2 (261 cm^{-1}), P3 (356 cm^{-1}), and P4 (417 cm^{-1}) with respect to Cr concentration. At low Cr doping ($x \leqslant 0.05$) in CRO, the value of ω_{ph} increases ($\sim 17\%$) for all (P1–P4) peaks, and remains constant at higher Cr concentration ($x \geqslant 0.05$). This blue shift (moving ω_{ph} towards higher value) in the more prominent peaks: P1–P3 [related to inter-(Ru/Cr)O$_6$ bending, stretching, and rotation] and P4 [related to intra-(Ru/Cr)O$_6$ bending] is due to the decrease ionic radii of Ru-site ion. This suggests that the Cr doping modifies the local bonding between ions due to structural distortion.

In order to further investigate the role of structural distortion in the magnetic ordering, the low temperature Raman spectra are carefully collected for CRCO15, in the 80–400 K temperature range. There is also no change in the spectral feature (no new peak) observed, indicating no structural phase transition in the investigated temperature range. All Raman spectra at various temperatures are analyzed using the Lorentzian multifunction (peaks P1–P8) to extract phonon parameters (frequency and linewidth) as a function of temperature. The ω_{ph} (T) dependency of pronounced Raman lines P1, P2, P3, and P4, are plotted in Fig. 3(d). The atomic displacement for $A_g(3)$ (P2) and $A_g(6)$ (P4) modes are schematically shown in the inset of Fig. 3(c). The change in the phonon frequency with temperature depends on several factors: unit cell volume expansion, intrinsic anharmonicity at constant unit cell volume, and spin-phonon coupling. The value of ω_{ph} decreases gradually below ~ 100 K, for all prominent peaks, suggesting the deviation from an anharmonic contribution. For fully anharmonic phonon-phonon scattering, the phonon frequency as a function of temperature is provided by the equation [48,49]:

$$\omega_{anh}(T) = \omega_0 + A \left[1 + \frac{2}{e^{\frac{\hbar \omega_0}{2k_B T}} - 1} \right], \qquad (3)$$

where ω_0 is the frequency of a phonon at absolute zero temperature A is an anharmonic coefficient, $\hbar$ is the reduced Planck constant, and k_B is the Boltzmann constant. The fitting value of ω_0 is 165 cm^{-1} for P1. In the absence of structural phase transition (all NPD patterns are fitted by
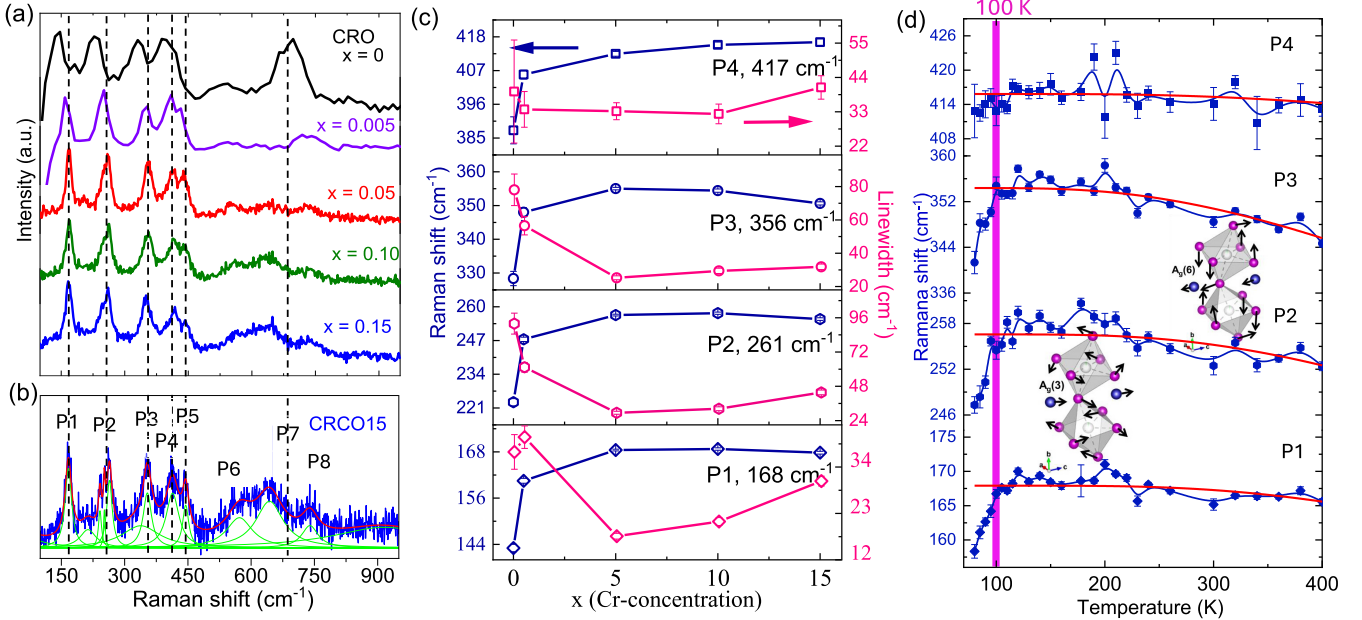
FIG. 3. (a) Room temperature Raman spectra of CRCO samples. (b) Lorentzian peaks (P1–P8) fitting shown for CRCO15 Raman spectra. (c) Variation of Raman shift (left y axis) and linewidth (right y axis) with respect to Cr concentration. (d) Variation of Raman shift and linewidth of P1, P2, P3, and P4 peaks, over the temperatures range 80–400 K. The solid red line is the fitting of Eq. (3). Inset shows the schematic picture of atomic displacement for $A_g(3)$ and $A_g(6)$ modes.

Pnma symmetry) down to 5 K, this deviation from the anharmonic contribution below ~100 K in CRCO15 attributes the spin-phonon coupling. Such spin-phonon interactions below ~100 K establish magnetic ordering in CRCO15.

C. Magnetic measurement

The field cooled (FC) magnetization data for CRCO15 measured at various applied fields: 0.05, 0.5, and 5 kOe, are shown in Fig. 4(a). The ordering temperature (T_C) is evaluated by fitting the magnetization data taken at lowest field with the following scaling law:

$$M(T) \sim (T_c - T)^\beta. \tag{4}$$

The fitting gives the value of T_C ~ 100 K and β ~ 0.9 near the phase transition. Such a large value of β was noticed for Sr-doped CaRuO$_3$ system [50], which cannot be described

by any known classical standard models. This value may be possibly explained by a strong disorder due to quantum fluctuation near phase transition [51]. The magnetic moment attains a maximum value at the lowest temperature (4 K). The value of magnetic moment at 4 K increases with increasing the applied field, giving an idea of the PM background of free Ru ions like in parent compound CRO. However, looking at the low-temperature thermal evolution of magnetization of the system at different fields. It is important to note that the low-temperature magnetization gets reduced with the increase in temperature. This is usually observed in the case of an itinerant ferromagnet, both by thermally excited magnons (following Bloch $A_{SW}T^{3/2}$ law) as well as Stoner excitations (following $B_{SE}T^2$ law) [52]. The obtained value of spin-wave stiffness constant (A_{SW}) and stoner excitation parameter (B$_{SE}$)
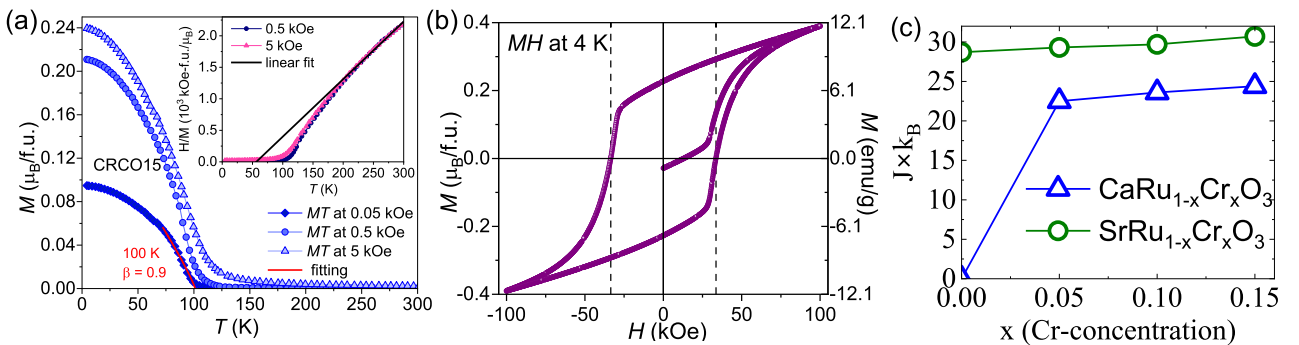

FIG. 4. (a) Temperature-dependent FC magnetization curve for CRCO15 at 0.05, 0.5, and 5 kOe applied field. Here, the red line shows the fitting of Eq. (4). The inset figure shows the inverse susceptibility (H/M) at 0.5 and 5 kOe. The black solid line shows the linear fitting in high-temperature PM region. (b) Magnetic hysteresis loop for CRCO15 at 4 K. The left and right y axis of the *MH* graph show the magnetization in μ_B/f.u. and emu/g, respectively. (c) Variation of the exchange constant $J \times k_B$ with Cr concentration in (Ca/Sr)Ru$_{1-x}$Cr$_x$O$_3$.

for CRCO15 is $1.7 \times 10^{-4}\,K^{-3/2}$ and $5.8 \times 10^{-5}\,K^{-2}$, respectively. These values are close to the reported values for itinerant ferromagnet SrRuO$_3$ [53], which indicates the possibilities of forming a ferromagnetic order in CRCO15. The inset of Fig. 4(a) depicts the inverse dc magnetic susceptibility plot at 0.5 kOe and 5 kOe fields, both showing a nonlinear behavior in the PM region (above the T_C). The nonlinearity downturn in the inverse dc magnetic susceptibility suggests the presence of Griffith's phases (GP) [54,55] in the Cr-doped samples. The nonlinear downturn softens at the higher field [see inset of Fig. 4(a)], which is a typical signature of the GP [56]. The strength of GP is explicitly characterized by the relation: $\chi^{-1} \propto (T - T_c)^{1-\lambda}$, where $0 \leqslant \lambda \leqslant 1$ is the susceptibility exponent. The observed decrease in the value of λ from 0.96 (for $x = 0.05$) to 0.78 (for $x = 0.15$) indicates a weakening of the GP with increasing Cr doping. This behavior is similarly reported in other doped perovskites [57]. Recent work also examines the GP and the evolution of magnetism in Cr-doped CRO [29].

Further, the $M(H)$ measurement is employed on CRCO15 at 4 K as shown in Fig. 4(b). The negative value of magnetization in the virgin curve (the first magnetization curve after cooling), could be considered as an error or an artifact of the negative field cooling process. It does not reflect the intrinsic magnetic properties of the material. Importantly, the hysteresis loop of magnetization is not getting saturated even up to 100 kOe applied field. This nonsaturating behavior along with a substantial coercive field ($\pm$ 33 kOe) indicates a large magnetocrystalline anisotropy in CRCO15. Important to note that the magnetic moment at 100 kOe is only $\sim$0.4 μ_B/f.u. The reduction of magnetization compared to SrRuO$_3$ ($\sim$1.6 μ_B/f.u.) has multiple origins: high coercive field, presence of significant magnetic disorders due to Cr^{3+} and Cr^{6+}, weaker exchange constant, etc. On Cr doping the lattice parameters along a, b, and c axes are reduced around 0.5%, 0.3%, and 0.1%, respectively [29]. The change in the lattice parameters with Cr doping up to 15% is rather small. However, such change in the lattice parameters together with temperature-induced structural modulations, which can alter the magnetic ground state from paramagnetic to ferromagnetic in CRO. This is also reflected in the evolution of exchange constant, which is estimated from the low-temperature $M(T)$ fitting for various Cr-doped samples. Figure 4(c) shows evolution of the exchange constant with Cr doping. A gradual evolution of ferromagnetism is evident from this plot. It is interesting to notice that the exchange constant for 15% Cr-doped sample is comparable with isostructural itinerant ferromagnet SrRuO$_3$. But the magnetization value is small compared to SrRuO$_3$ due to the magnetic disorder and mixed valency of Cr discussed in the recent works [28,29]. Now, it is curious to know the microscopic origin of such complex magnetism and the evolution of crystal structure, with temperature.

D. Temperature-dependent neutron diffraction and neutron depolarization

The T (5–300 K)-dependent NPD for CRO and CRO15 compounds are collected. The Rietveld analysis of NPD for both the compounds suggests there is no structural phase transition down to 5 K. The values of lattice parameters along all three crystallographic directions and unit cell volume are evaluated at various T for both samples. Figures 5(a), 5(b), and 5(c) depict the normalized lattice parameters: $a/a_{300\,K}$, $c/c_{300\,K}$, $b/b_{300\,K}$, and unit cell volume of CRCO15 (solid symbol) in comparison with CRO (open symbol). In the case of the parent compound the $a/a_{300\,K}$ value is almost constant throughout the temperature range. However, for CRCO15 the value of $a/a_{300\,K}$ shows a steplike increment ($\sim$0.1%) close to the $T_C \sim 100$ K and then remains constant below 100 K. Interestingly, $c/c_{300\,K}$ shows a gradual decreasing trend with lowering T for both samples. In addition to the downtrend in $c/c_{300\,K}$ value, a similar steplike increment is also noticed for CRCO15 at $\sim$100 K. Below 100 K it remains constant down to 5 K. In (Ca/Sr)RuO$_3$ system, it is reported that the lattice volume below a certain temperature (often below T_C) is constant known as Invar effect [58] where lattice distortion counteracts the usual thermal expansivity. We find that the Invar effect also persists in CaRuO$_3$ with Cr doping. However, the sudden increment ($\sim$0.1%) of a and c lattice parameters upon cooling from 150–100 K is correlated with the octahedral distortion (mainly Σ, discussed later), especially in the 100–150 K region.

The value of $b/b_{300\,K}$ shows a decreasing trend with lowering T down to 100 K. Below $\sim$100 K it remains unchanged for CRO, but shows concave upward for CRCO15. The overall effect of temperature, as well as Cr doping on the crystal structure, can be visualized from $V/V_{300\,K}$ vs T plot of both samples. As we move towards lower T, the value of the $V/V_{300\,K}$ decreases down to $\sim$150 K for CRCO15. Below 150 K the relative volume of CRCO15 increases and attains a peak at $\sim$100 K, whereas, no such change is observed for the parent compound CRO. Such a peak in temperature-dependent unit cell volume has been reported earlier for a 15% Fe-doped CRO system at the Curie temperature [59]. Thus, the peak at $\sim$100 K is attributed to the magnetic ordering of CRCO15 (matched with T_C observed from the magnetization data) and reveals a magnetostriction effect [60]. The derived values of lattice parameters at 5 K for both samples are tabulated in Table I. Surprisingly, there is no magnetic Bragg's peak observed in the NPD of CRCO15 below $T_C \sim 100$ K. This contradicts the fact that the peak in the volume corresponds to the magnetic ordering. In contrast, in isostructural Cr-doped SrRuO$_3$, a magnetic Bragg peak has been observed at 1.6 Å^{-1} below $T_C \sim 190$ K [28]. The absence of a magnetic peak in the NPD of CRCO15 is attributed to the low value of magnetic moment as found from M vs H measurement at 4 K ($\sim$0.4 μ_B/f.u. at 100 kOe) and this value is below the measurement limit of the PD-1. Thus, to understand the magnetic phase transitions in detail, one dimensional ND experiments have been conducted on both CRO and CRCO15. Figure 5(d) demonstrates the comparative T-dependent ND curves of CRO and CRCO15. For the parent compound CRO, there is no neutron beam depolarization observed down to 2 K. Whereas, the CRCO15 exhibits a significant amount $\sim$14% of neutron beam depolarization below $T_C \sim 100$ K, suggesting a finite magnetization of the domain. A depolarization of the neutron beam is expected in a system when magnetic domains/patches are sufficiently large, long lived, and uniform magnetization is sufficiently large [31]. This confirms a long-ranged magnetic ordering in the CRCO15. The origin
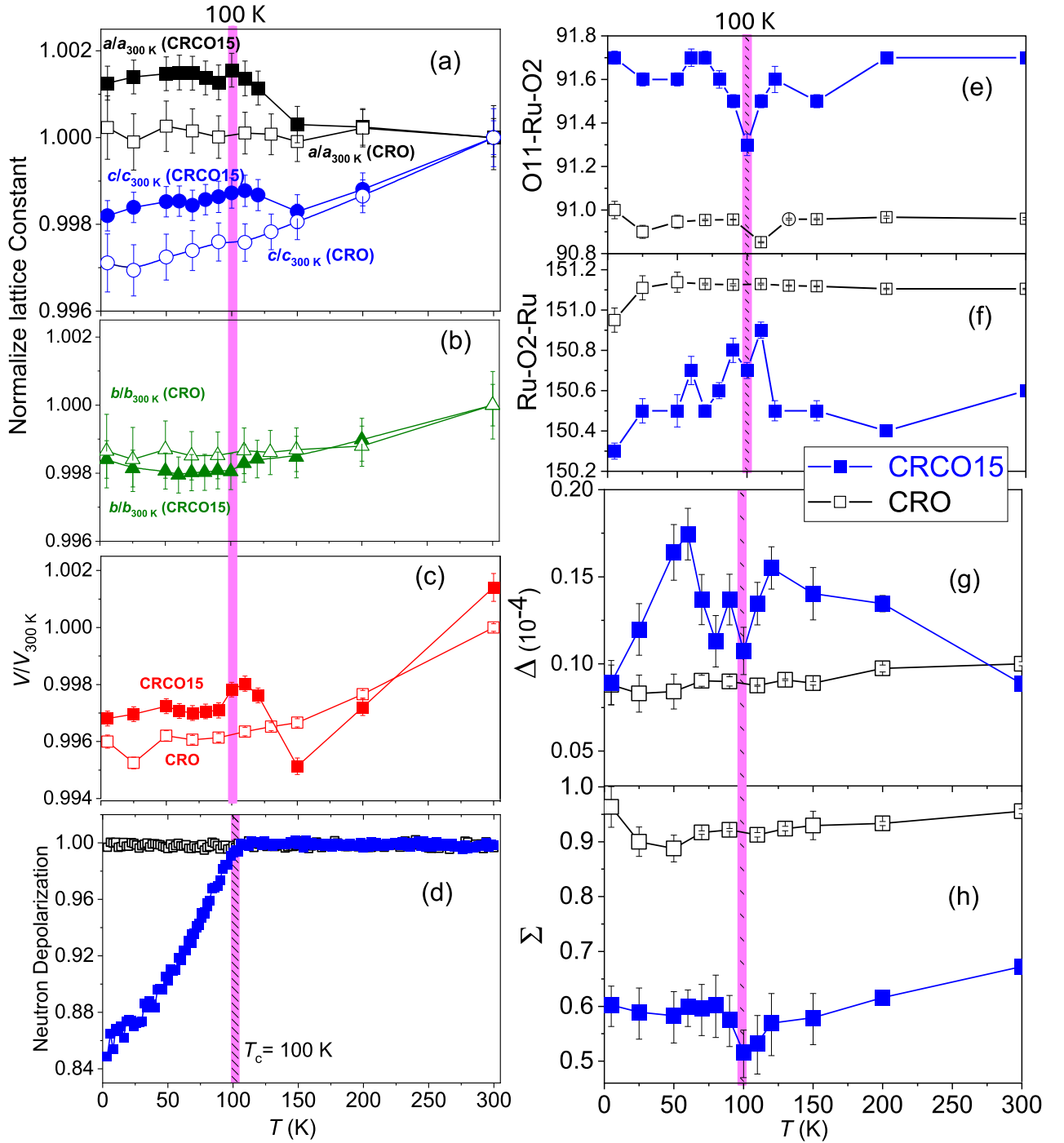
FIG. 5. The temperature variation of the normalized (a), (b) lattice parameters (with respect to 300 K), and (c) unit cell volumes, of CRO and CRCO15 compounds. Error bars in volume is smaller than the data point size. (d) The temperature-dependent transmitted neutron beam depolarization measured during the warming cycle under 35 Oe magnetic field. Temperature evolution of various parameters of $(Ru/Cr)O_6$ octahedron; (e) O11-Ru-O2 bond angles, (f) Ru-O2-Ru bond angles between neighboring RuO_6 octahedron, (g) stretching octahedral distortion, and (h) angular octahedral distortion. In all plots a open symbol is used for CRO and a solid symbol for CRCO15 compounds.

of such induced ferromagnetism in $CaRuO_3$ is twofold: (i) Cr doping reduces the orthorhombicity and squeezes the unit cell volume, (ii) the temperature-driven structural modulation with an anomaly observed in the bond angles, distortions around T_C. Both these factors effectively install ferromagnetic exchange in $CaRuO_3$. Figures 5(e) and 5(f) depict the

variation of intra-O11-Ru-O2 and inter-Ru-O2-Ru octahedral bond angle with respect to T. Both bond angles remain constant within the entire temperature range for pure compounds, whereas CRCO15 shows anomaly at ~100 K. The changes in the octahedral bond lengths and bond angles with respect to T are quantified in terms of octahedral distortions [Δ, Σ as

defined in Eqs. (1), (2)]. Figures 5(g), 5(h) depicts the variation of Δ and Σ vs T for CRCO15 compared with CRO. A weak anomaly in Δ and Σ is evident for $x = 0.15$ around T_C, which is not present in the parent compound. This clearly indicates that the anomalies are associated with the magnetic ordering and making a case for the magnetostructural coupling. In a nutshell, the comprehensive T-dependent NPD and ND analysis reveal the presence of structural modulations around the magnetic ordering temperature ~ 100 K, which play an important role in stabilizing FM ordering in CRCO15. Such structural anomalies and ND are absent in the case of parent compound CRO.

IV. CONCLUSION

Temperature-dependent NPD of CRO and CRCO15 suggests the orthorhombic crystal structure with *Pnma* space group symmetry. Nevertheless, Cr doping in CRO reduces the orthorhombicity factor (a/c) and the unit cell volume. Moreover, the Cr doping increases the value of octahedral tilt θ and stretching distortions Δ by $\sim 6°$ and 18 times (at 15% Cr doping in CRO), respectively. Because of the alteration in the ionic radii of the same site, Cr doping modifies the Raman modes associated with the $(Ru/Cr)O_6$ octahedral distortion. With a modest (0.5%) Cr doping in CRO, the maximum increase in Raman frequency, or blue shift ($\sim 17\%$) of Raman peaks P1–P4, is found. This shift is related to the asymmetric stretching, bending, and rotation of the $(Ru/Cr)O_6$ octahedra $[A_g(1), A_g(3)]$ and the position of the Ca atom $[A_g(5)]$ (see Table II). Such modest Cr doping is sufficient to stabilize FM order in CRO, which is situated on the verge of FM ordering, revealing a strong correlation between the crystal structure distortion and magnetic ordering. Below ~ 100 K, a gradual decrease in the Raman frequency of P1–P4 peaks is observed in CRCO15. There can be magnetic disorder due to mixed valency of transition-metal ions (Ru/Cr) affecting crystal's original anharmonicity in the whole measurement range of temperature. However, below the Curie temperature, the spin-phonon coupling becomes the dominant factor of phonon incoherence as disorder and inhomogeneity found to be independent of the temperature. The crystal structure prevails orthorhombic (*Pnma*) at all temperatures (300–5 K), confirmed by the NPD study. Absence of any structural phase transition confirms that the spin-phonon coupling is the origin for the deviation of phonon frequency from the expected anharmonic trend below 100 K, in CRCO15. The magnetization data confirms the FM ordering in CRCO15 below $T_C \sim 100$ K. The low magnetic moment value [~ 0.4 μ_B/f.u., is 14% of an effective spin only moment of CRCO15 (2.88 μ_B/f.u.)] even at 100 kOe indicating inhomogeneous exchange interaction between the Ru and Cr ions owing to their distinct ionic sizes and valence states. Interestingly, no magnetic Bragg's peak is found in the NPD of both compounds down to 5 K. It is explained by the low magnetic moment value in the case of CRCO15, which is below the measurement limit of PD-1. However, the magnetic ordering below about 100 K is confirmed by a change in the ND in CRCO15, which is absent in case of the parent compound CRO. Nevertheless, the temperature-dependent NPD investigations in CRCO15 reveal structural modulation near the $T_C = 100$ K due to the setting up of the FM ordering in CRCO15. In contrast, no such anomalies are found for the parent compound CRO due to having a spin-disordered (paramagnetic) ground state. This work demonstrates that the Cr doping effectively installs ferromagnetism in $CaRuO_3$ by means of temperature-dependent structural modulations.

[1] A. M. Glazer, Perovskites modern and ancient, Struct. Sci. **58**, 1075 (2002).

[2] W. Witczak-Krempa, G. Chen, Y. B. Kim, and L. Balents, Correlated quantum phenomena in the strong spin-orbit regime, Annu. Rev. Condens. Matter Phys. **5**, 57 (2014).

[3] Y. Y. Chin, Z. Hu, H.-J. Lin, S. Agrestini, J. Weinen, C. Martin, S. Hébert, A. Maignan, A. Tanaka, J. Cezar, N. B. Brookes, Y.-F. Liao, K.-D. Tsuei, C. T. Chen, D. I. Khomskii, and L. H. Tjeng, Spin-orbit coupling and crystal-field distortions for a low-spin $3d^5$ state in $BaCoO_3$, Phys. Rev. B **100**, 205139 (2019).

[4] M. A. Zeb and H.-Y. Kee, Interplay between spin-orbit coupling and Hubbard interaction in $SrIrO_3$ and related Pbnm perovskite oxides, Phys. Rev. B **86**, 085149 (2012).

[5] J. Longo, P. Raccah, and J. Goodenough, Magnetic properties of $SrRuO_3$ and $CaRuO_3$, J. Appl. Phys. **39**, 1327 (1968).

[6] K. Aleksandrov and J. Bartolomé, Structural distortions in families of perovskite-like crystals, Phase Trans.: A Multinat. J. **74**, 255 (2001).

[7] E. Maksimov, N. Matsko, S. Ebert, and M. Magnitskaya, Some problems in the theory of perovskite ferroelectrics, Ferroelectrics **354**, 19 (2007).

[8] M. W. Lufaso and P. M. Woodward, Jahn–Teller distortions, cation ordering and octahedral tilting in perovskites, Acta Crystallogr. Sect. B: Struct. Sci. **60**, 10 (2004).

[9] A. M. Glazer, The classification of tilted octahedra in perovskites, Acta Crystallogr. B: Struct. Crystallogr. Cryst. Chem. **28**, 3384 (1972).

[10] H. T. Dang, J. Mravlje, A. Georges, and A. J. Millis, Electronic correlations, magnetism, and Hund's rule coupling in the ruthenium perovskites $SrRuO_3$ and $CaRuO_3$, Phys. Rev. B **91**, 195149 (2015).

[11] L. Abbes and H. Noura, Perovskite oxides $MRuO_3$ (M = Sr, Ca and Ba): Structural distortion, electronic and magnetic properties with GGA and GGA-modified becke-johnson approaches, Results Phys. **5**, 38 (2015).

[12] C. S. Alexander, G. Cao, V. Dobrosavljevic, S. McCall, J. E. Crow, E. Lochner, and R. P. Guertin, Destruction of the Mott insulating ground state of Ca_2RuO_4 by a structural transition, Phys. Rev. B **60**, R8422 (1999).

[13] G. Cao, O. Korneta, S. Chikara, L. DeLong, and P. Schlottmann, Non-Fermi-liquid behavior in single-crystal $CaRuO_3$: Comparison to ferromagnetic $SrRuO_3$, Solid State Commun. **148**, 305 (2008).

[14] T. Kiyama, K. Yoshimura, K. Kosuge, H. Michor, and A. Gerfried Hilscher, Specific heat of $(Sr - Ca)RuO_3$, J. Phys. Soc. Jpn. **67**, 307 (1998).

[15] H. Mukuda, K. Ishida, Y. Kitaoka, K. Asayama, R. Kanno, and M. Takano, Spin fluctuations in the ruthenium oxides RuO_2, $SrRuO_3$, $CaRuO_3$, and Sr_2RuO_4 probed by Ru NMR, Phys. Rev. B **60**, 12279 (1999).

[16] T. He and R. Cava, Disorder-induced ferromagnetism in $CaRuO_3$, Phys. Rev. B **63**, 172403 (2001).

[17] H. Kojitani, Y. Shirako, and M. Akaogi, Post-perovskite phase transition in $CaRuO_3$, Physics of the Earth and Planetary Interiors **165**, 127 (2007).

[18] I. I. Mazin and D. J. Singh, Electronic structure and magnetism in Ru-based perovskites, Phys. Rev. B **56**, 2556 (1997).

[19] Y. Chen, J. Zhou, F.-X. Wu, W.-J. Ji, S.-T. Zhang, Y.-F. Chen, and Y.-Y. Zhu, Microstructure and ferromagnetic property in $CaRuO_3$ thin films with pseudoheterostructure, Appl. Phys. Lett. **96**, 182502 (2010).

[20] T. He and R. Cava, The effect of Ru-site dopants on the magnetic properties of $CaRuO_3$, J. Phys.: Condens. Matter **13**, 8347 (2001).

[21] S. Taniguchi, M. Ogawara, N. Fukuoka, S. Mizusaki, Y. Nagata, Y. Noro, and H. Samata, Ferromagnetism of epitaxially grown $CaRu_{1-x}M_xO_3(M = Ti, Mn)$ films, J. MMM **321**, 3335 (2009).

[22] A. Maignan, B. Raveau, V. Hardy, N. Barrier, and R. Retoux, Ferromagnetism induced by chromium substitution in the $CaRuO_3$ perovskite, Phys. Rev. B **74**, 024410 (2006).

[23] V. Durairaj, S. Chikara, X. N. Lin, A. Douglass, G. Cao, P. Schlottmann, E. S. Choi, and R. P. Guertin, Highly anisotropic magnetism in Cr-doped perovskite ruthenates, Phys. Rev. B **73**, 214414 (2006).

[24] T. Taniguchi, S. Mizusaki, N. Okada, Y. Nagata, S. H. Lai, M. D. Lan, N. Hiraoka, M. Itou, Y. Sakurai, T. C. Ozawa, Y. Noro, and H. Samata, Crystallographic and magnetic properties of the mixed-valence oxides $CaRu_{1-x}Mn_xO_3$, Phys. Rev. B **77**, 014406 (2008).

[25] G. Cao, S. McCall, J. Bolivar, M. Shepard, F. Freibert, P. Henning, J. E. Crow, and T. Yuen, Itinerant-to-localized electron transition in $CaRu_{1-x}Sn_xO_3$ and $SrRu_{1-x}Pb_xO_3$, Phys. Rev. B **54**, 15144 (1996).

[26] D. K. Singh, A. Ernst, V. Dugaev, Y. Chen, and J. Gunasekera, Quantum magnetic properties and metal-to-insulator transition in chemically doped calcium ruthenate perovskite, Physica Status Solidi (b) **259**, 2100503 (2022).

[27] L. Wang, L. Hua, and L. Chen, First-principles investigation of Cr doping effects on the structural, magnetic and electronic properties in $SrRuO_3$, Solid State Commun. **150**, 1069 (2010).

[28] Pooja, B. Saha, N. Choudhary, P. K. Maji, A. K. Bera, S. M. Yusuf, and C. Sow, Structural modulation driven curie temperature enhancement in Cr-doped $SrRuO_3$, Phys. Rev. B **109**, 144404 (2024).

[29] P. Kesarwani, S. N. Sarangi, D. Samal, and C. Sow, Evolution of ferrimagnetism against Griffiths singularity in calcium ruthenate, J. Phys.: Condens. Matter **36**, 265603 (2024).

[30] G. Shirane, S. M. Shapiro, and J. M. Tranquada, *Neutron Scattering with a Triple-Axis Spectrometer: Basic Techniques* (Cambridge University Press, Cambridge, 2002).

[31] M. Seifert, P. Schmakat, M. Schulz, P. Jorba, V. Hutanu, C. Geibel, M. Deppe, and C. Pfleiderer, Neutron depolarization due to ferromagnetism and spin freezing in $CePd_{1-x}Rh_x$, Phys. Rev. Res. **4**, 043029 (2022).

[32] S. M. Yusuf, L. M. Rao, R. Mukhopadhyay, S. Giri, K. Ghoshray, and A. Ghoshray, Low temperature magnetic phase of $KMnFeF_6$: A neutron depolarisation and diffraction study, Solid State Commun. **101**, 145 (1997).

[33] C. Pfleiderer, P. Böni, C. Franz, T. Keller, A. Neubauer, P. Niklowitz, P. Schmakat, M. Schulz, Y.-K. Huang, J. Mydosh *et al.*, Search for electronic phase separation at quantum phase transitions, J. Low Temp. Phys. **161**, 167 (2010).

[34] H. Bakker, M. Rekveldt, and J. Van Loef, Neutron depolarization measurements in nickel near the curie point, Phys. Lett. A **27**, 69 (1968).

[35] M. Takahashi, S. Itoh, and M. Takeda, Neutron depolarization study on the magnetic critical fluctuation in Rb_2CrCl_4, J. Phys. Soc. Jpn. **64**, 268 (1995).

[36] J. Orenstein and A. Millis, Advances in the physics of high-temperature superconductivity, Science **288**, 468 (2000).

[37] W. Eerenstein, N. Mathur, and J. F. Scott, Multiferroic and magnetoelectric materials, Nature (London) **442**, 759 (2006).

[38] J. Menéndez, Characterization of bulk semiconductors using raman spectroscopy, *Raman Scattering in Materials Science* (Springer, Berlin, 2000).

[39] M. N. Iliev, A. P. Litvinchuk, H. G. Lee, C. L. Chen, M. L. Dezaneti, C. W. Chu, V. G. Ivanov, M. V. Abrashev, and V. N. Popov, Raman spectroscopy of $SrRuO_3$ near the paramagnetic-to-ferromagnetic phase transition, Phys. Rev. B **59**, 364 (1999).

[40] S. Paranjpe and Y. Dande, A neutron diffractometer with a linear position sensitive detector, Pramana **32**, 793 (1989).

[41] C. Ritter, Neutrons not entitled to retire at the age of 60: More than ever needed to reveal magnetic structures, in *Solid State Phenomena*, Vol. 170 (Trans Tech, Warwick, 2011), pp. 263–269.

[42] S. M. Yusuf and L. M. Rao, Magnetic studies in mesoscopic length scale using polarized neutron spectrometer at Dhruva reactor, Trombay, Pramana **47**, 171 (1996).

[43] K. Momma and F. Izumi, Vesta: A three-dimensional visualization system for electronic and structural analysis, J. Appl. Crystallogr. **41**, 653 (2008).

[44] W. Lu, W. Dong Song, K. He, J. Chai, C.-J. Sun, G.-M. Chow, and J.-S. Chen, The role of octahedral tilting in the structural phase transition and magnetic anisotropy in $SrRuO_3$ thin film, J. Appl. Phys. **113**, 063901 (2013).

[45] N. Kolev, C. L. Chen, M. Gospodinov, R. P. Bontchev, V. N. Popov, A. P. Litvinchuk, M. V. Abrashev, V. G. Hadjiev, and M. N. Iliev, Raman spectroscopy of $CaRuO_3$, Phys. Rev. B **66**, 014101 (2002).

[46] M. N. Iliev, M. V. Abrashev, H. G. Lee, V. N. Popov, Y. Y. Sun, C. Thomsen, R. L. Meng, and C. W. Chu, Raman spectroscopy of orthorhombic perovskitelike $YMnO_3$ and $LaMnO_3$, Phys. Rev. B **57**, 2872 (1998).

[47] G. Gou, I. Grinberg, A. M. Rappe, and J. M. Rondinelli, Lattice normal modes and electronic properties of the correlated metal $LaNiO_3$, Phys. Rev. B **84**, 144101 (2011).

[48] M. Balkanski, R. F. Wallis, and E. Haro, Anharmonic effects in light scattering due to optical phonons in silicon, Phys. Rev. B **28**, 1928 (1983).

[49] B. Poojitha, A. Shaji, S. Badola, and S. Saha, Spin–phonon coupling in ferrimagnet spinel $CoMn_2O_4$, J. Chem. Phys. **156**, 184701 (2022).

[50] R. Roshko, C. Viddal, and W. Li, Critical behaviour and irreversibility in $Ca_xSr_{1-x}RuO_3$, Phys. B: Condens. Matter **343**, 30 (2004).

[51] D. Fuchs, M. Wissinger, J. Schmalian, C.-L. Huang, R. Fromknecht, R. Schneider, and H. v. Löhneysen, Critical scaling analysis of the itinerant ferromagnet $Sr_{1-x}Ca_xRuO_3$, Phys. Rev. B **89**, 174405 (2014).

[52] T. Okabe, Spin wave and stability of the double exchange ferromagnet, Prog. Theor. Phys. **97**, 21 (1997).

[53] C. Sow, D. Samal, P. S. A. Kumar, A. K. Bera, and S. M. Yusuf, Structural-modulation-driven low-temperature glassy behavior in $SrRuO_3$, Phys. Rev. B **85**, 224426 (2012).

[54] R. B. Griffiths, Nonanalytic behavior above the critical point in a random Ising ferromagnet, Phys. Rev. Lett. **23**, 17 (1969).

[55] M. De Andrade, R. Chau, R. Dickey, N. Dilley, E. Freeman, D. Gajewski, M. Maple, R. Movshovich, A. C. Neto, G. Castilla *et al.*, Evidence for a common physical description of non-Fermi-liquid behavior in chemically substituted f-electron systems, Phys. Rev. Lett. **81**, 5620 (1998).

[56] A. Bray and M. Moore, On the eigenvalue spectrum of the susceptibility matrix for random spin systems, J. Phys. C **15**, L765 (1982).

[57] S. M. Zhou, Y. Li, Y. Q. Guo, J. Y. Zhao, X. Cai, and L. Shi, Observation of a Griffiths-like phase in ca-doped cobaltites, J. Appl. Phys. **114**, 163903 (2013).

[58] T. Kiyama, K. Yoshimura, K. Kosuge, Y. Ikeda, and Y. Bando, Invar effect of $SrRuO_3$: Itinerant electron magnetism of Ru 4d electrons, Phys. Rev. B **54**, R756 (1996).

[59] T. Taniguchi, S. Mizusaki, N. Okada, Y. Nagata, K. Mori, T. Wuernisha, T. Kamiyama, N. Hiraoka, M. Itou, Y. Sakurai *et al.*, Anomalous volume expansion in $CaRu_{0.85}Fe_{0.15}O_3$: Neutron powder diffraction and magnetic compton scattering, Phys. Rev. B **75**, 024414 (2007).

[60] R. Ranjan, R. Garg, A. Senyshyn, M. Hegde, H. Ehrenberg, and H. Boysen, Magneto-structural study of a Cr-doped $CaRuO_3$, J. Phys.: Condens. Matter **21**, 326001 (2009).